

Deblur4DGS: 4D Gaussian Splatting from Blurry Monocular Video

Renlong Wu, Zhilu Zhang, Mingyang Chen, Zifei Yan, Wangmeng Zuo
hirenlongwu@gmail.com, cszlhong@outlook.com, youngmchan269@gmail.com,
yanzifei@hit.edu.cn, wmzuo@hit.edu.cn
Harbin Institute of Technology

Abstract

Recent 4D reconstruction methods have yielded impressive results but rely on sharp videos as supervision. However, motion blur often occurs in videos due to camera shake and object movement, while existing methods render blurry results when using such videos for reconstructing 4D models. Although a few approaches attempted to address the problem, they struggled to produce high-quality results, due to the inaccuracy in estimating continuous dynamic representations within the exposure time. Encouraged by recent works in 3D motion trajectory modeling using 3D Gaussian Splatting (3DGS), we take 3DGS as the scene representation manner, and propose Deblur4DGS to reconstruct a high-quality 4D model from blurry monocular video. Specifically, we transform continuous dynamic representations estimation within an exposure time into the exposure time estimation. Moreover, we introduce the exposure regularization term, multi-frame, and multi-resolution consistency regularization term to avoid trivial solutions. Furthermore, to better represent objects with large motion, we suggest blur-aware variable canonical Gaussians. Beyond novel-view synthesis, Deblur4DGS can be applied to improve blurry video from multiple perspectives, including deblurring, frame interpolation, and video stabilization. Extensive experiments in both synthetic and real-world data on the above four tasks show that Deblur4DGS outperforms state-of-the-art 4D reconstruction methods. The codes will be publicly available.

Introduction

Substantial efforts have been made for 4D reconstruction, which has extensive applications in augmented reality and virtual reality. To model static scenes, Neural Radiance Field (NeRF) (Mildenhall et al. 2021) and 3D Gaussian Splatting (3DGS) (Kerbl et al. 2023) propose implicit neural representation manner and explicit Gaussian ellipsoids one, respectively. To model dynamic objects, implicit neural fields (Zhu et al. 2024; Yang et al. 2024; Wu et al. 2024; Yan, Li, and Lee 2023) and explicit deformation (Duan et al. 2024b; Chu, Ke, and Fragkiadaki 2024; Katsumata, Vo, and Nakayama 2024; Lin et al. 2024b; Li et al. 2024; Wang et al. 2024) are suggested for motion representation. While achieving great progress, most methods rely on synchronized multi-view videos. They yield unsatisfactory results when applied to monocular video, where dynamic objects are only observed once at each timestamp. To alleviate the under-constrained

nature of the problem, recent studies have introduced data-driven priors, such as depth maps (Lee et al. 2023c; Yang et al.), optical flows (Gao et al. 2024; Zhu et al. 2024), tracks (Seidenschwarz et al. 2024; Lei et al. 2024), and generative models (Wu et al. 2025; Chu, Ke, and Fragkiadaki 2024; Zeng et al. 2025) for better 4D reconstruction.

Unfortunately, motion blur often arises due to camera shake and object movement. When reconstructing the 4D scene from the blurry video, the above methods usually render blurry results. The first step to solving this problem is to deal with camera motion blur, which is relatively simple. Some NeRF-based (Lee et al. 2023a; Wang et al. 2023; Lee et al. 2023b) and 3DGS-based (Zhao, Wang, and Liu 2024; Chen and Liu 2024; Oh et al. 2024) methods have suggested jointly optimizing 3D representation and camera poses within the exposure time by calculating the reconstruction loss between the synthetic blurry images and the input blurry frames. In contrast, the object motion blur is more challenging to address, as the solution has to estimate continuous and sharp dynamic representations within the exposure time to simulate blurry frames.

In this work, we take 3DGS (Kerbl et al. 2023) as the scene representation manner to explore the problem, driven by two main motivations. First, its successful application in 4D reconstruction make this method highly promising. Second, the explicit 3D motion modeling presents an opportunity to simplify the complex continuous dynamic representations estimation within the exposure time into exposure time estimation, avoiding complex extra motion modeling in DyBluRF (Sun et al. 2024a; Bui et al. 2023). Once the exposure time is estimated, continuous dynamic representations can be obtained by directly interpolating between representations at the nearest integer timestamps. We note that the concurrent work BARD-GS (Lu et al. 2025) adopts a similar strategy, but they perform unsatisfactorily due to the under-constrained optimization, especially for large object motion.

Specifically, we propose Deblur4DGS, a Gaussian Splatting framework for 4D reconstruction from blurry monocular video. For the static scene, we jointly optimize the camera poses at exposure start and end with static Gaussians. For the dynamic objects, we optimize learnable exposure time parameters and dynamic Gaussians of the integer timestamps, simultaneously. Then continuous camera poses and dynamic Gaussians within exposure time can be

obtained by interpolation, and they are used to render continuous sharp frames to calculate the reconstruction loss. Moreover, to avoid trivial solutions, we introduce the exposure regularization term, as well as the multi-frame and multi-resolution consistency regularization terms. Furthermore, existing 4D reconstruction methods generally select Gaussians at a single timestamp as canonical Gaussians. However, it may produce results with missing details in scenes with large motion, especially when processing blurry videos with a low frame rate. To alleviate this issue, we suggest variable canonical Gaussians as time progresses based on the image blur level. Gaussians corresponding to the sharper frame are selected as the canonical ones for better blur removal, and each canonical Gaussian is only used for nearby timestamps to reduce difficulty of modeling large motion.

Blurry videos suffer from not only motion blur, but also low frame rates and scene shake generally. Beyond novel-view synthesis, the optimized Deblur4DGS can be applied to address these problems, achieving deblurring, frame interpolation, and video stabilization. We evaluate Deblur4DGS from all four perspectives. Extensive experiments on both synthetic and real-world data demonstrate that Deblur4DGS outperforms state-of-the-art 4D reconstruction methods quantitatively and qualitatively while maintaining real-time rendering speed. Furthermore, Deblur4DGS has competitive capabilities in comparison with task-specific video processing models trained in a supervised manner.

The main contributions can be summarized as follows:

- We propose Deblur4DGS, a 4D Gaussian Splatting framework specially designed to reconstruct a high-quality 4D model from blurry monocular video.
- We propose transforming dynamic representation estimation into exposure time estimation, where a series of regularizations are suggested to tackle under-constrained optimization and blur-aware variable canonical Gaussians is present to better represent dynamic objects.
- Extensive experiments in synthetic and real-world data show that Deblur4DGS outperforms state-of-the-art 4D reconstruction methods on novel-view synthesis, deblurring, frame interpolation, and video stabilization tasks.

Related Work

Image and Video Deblurring

Deep learning-based image (Ren et al. 2023; Li et al. 2023; Kong et al. 2023; Wang et al. 2022; Zhang et al. 2022; Lin et al. 2024a; Zhang et al. 2024) and video (Zhong et al. 2023b; Liang et al. 2024; Pan et al. 2023; Zhang, Xie, and Yao 2024; Zhong et al. 2023a, 2020; Chan et al. 2022) deblurring methods have been widely explored. Compared to image deblurring methods, video ones leverage temporal clues between consecutive frames for more effective restoration. DBLRNet (Zhang et al. 2018a) employs spatial-temporal 3D convolution for spatial and temporal features aggregation. DSTNet (Pan et al. 2023) develops a deep discriminative spatial and temporal network. BasicVSR++ (Chan et al. 2022) improves feature fusion with second-order feature propagation and flow-guided alignment. BSSTNet (Zhang, Xie, and Yao 2024) introduces a

blur map to sufficiently utilize the entire video, achieving recent state-of-the-art. When reconstructing from a blurry video, pre-processing it with the 2D deblurring method is a straightforward manner. However, 2D deblurring methods cannot perceive 3D structures and maintain scene geometric consistency, leading to unsatisfactory scene reconstruction.

3D and 4D Reconstruction

To reconstruct 3D models, NeRF (Mildenhall et al. 2021) and 3DGS (Kerbl et al. 2023) introduce implicit neural representation manner and explicit Gaussian ellipsoids one respectively, where the latter generally achieves better results in both image quality and rendering speed. To reconstruct 4D models, most works (Somraj et al. 2024; Duan et al. 2024a; Lu et al. 2024; Luiten et al. 2023; Kratimenos, Lei, and Daniilidis 2023; Huang et al. 2024; Lin et al. 2024b; Li et al. 2024; Shaw et al.; Sun et al. 2024b; Wu et al. 2024; Yang et al. 2024; Bae et al. 2024; Mihajlovic et al. 2024; Duan et al. 2024b) incorporate implicit neural fields and explicit deformation for motion representation. For example, DeformableGS (Yang et al. 2024) achieves it with multi-layer perceptrons. 4DGasusians (Bae et al. 2024) improves it with a multi-resolution HexPlane (Cao and Johnson 2023). E-D3DGS (Wu et al. 2024) introduces per-Gaussian embeddings and temporal embeddings. Moreover, to better reconstruct from monocular video, some studies enhance 4D reconstruction with data-driven priors, such as depth maps (Lee et al. 2023c; Yang et al.), optical flows (Tian, Du, and Duan 2023; Gao et al. 2024), tracks (Wang et al. 2024; Seidenschwarz et al. 2024), and generative models (Wu et al. 2025; Chu, Ke, and Fragkiadaki 2024).

Note that these methods heavily rely on high-quality sharp videos for supervision and perform poorly when facing blurry inputs. To process camera motion in static areas, recent works (Lee et al. 2023a; Ma et al. 2022; Wang et al. 2023; Lee et al. 2023b, 2024a; Zhao, Wang, and Liu 2024; Peng et al. 2024a; Lee et al. 2024b; Chen and Liu 2024; Oh et al. 2024) suggest jointly optimizing the scene representation and recovering the camera poses within the exposure time. To process object motion blur in dynamic scenes, Dy-BluRF (Sun et al. 2024a; Bui et al. 2023) incorporates object motion blur formation into dynamic model optimization but faces challenges in producing high-quality images and achieving real-time rendering. In this work, with 3DGS as the scene representation manner, we develop Deblur4DGS to reconstruct a high-quality 4D model from a blurry video.

Preliminary

4D Gaussian Splatting

A 3D Gaussian (Kerbl et al. 2023) is parameterized by $\{\mathbf{x}, \mathbf{r}, \mathbf{s}, \alpha, \mathbf{c}\}$, where \mathbf{x} characterizes the center position in the world space, rotation matrix \mathbf{r} and scale matrix \mathbf{s} define the shape, α is opacity, and spherical harmonics (SH) coefficients \mathbf{c} represent the view-dependent color.

4D Gaussian Splatting (4DGS) usually process static and dynamic regions separately. Static regions can be represented by a set of 3D Gaussians, named \mathbf{S} . For the dynamic areas, 4DGS generally selects a timestamp (*e.g.*, the first

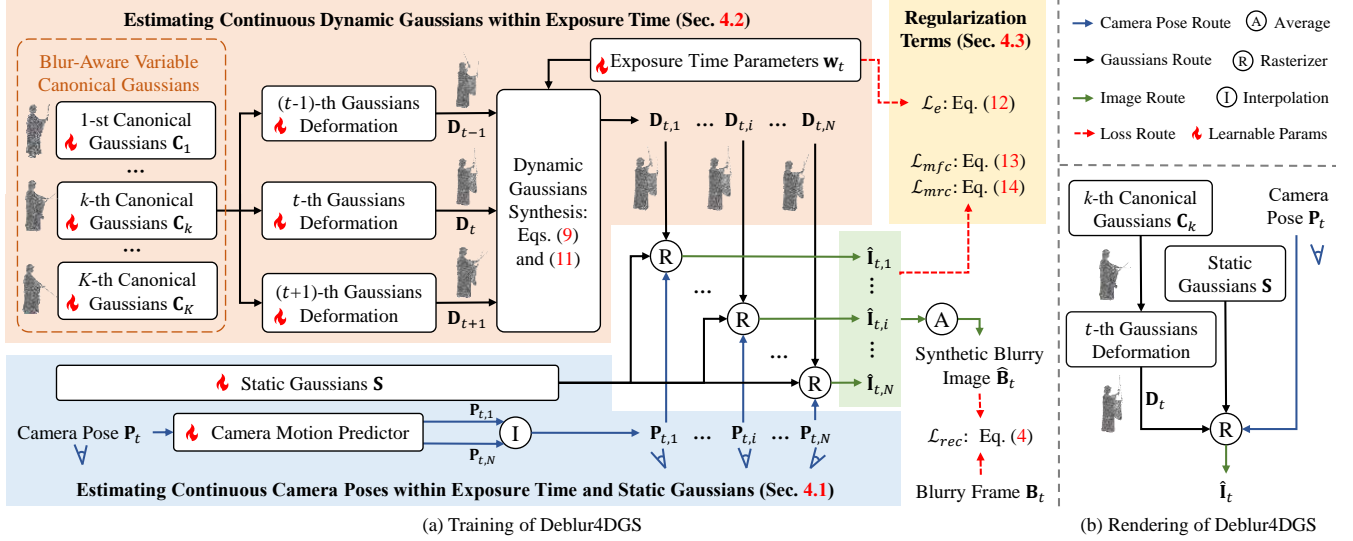


Figure 1: (a) Training of Deblur4DGS. When processing t -th frame, we first discretize its exposure time into N timestamps. Then, we estimate continuous camera poses $\{\mathbf{P}_{t,i}\}_{i=1}^N$ and dynamic Gaussians $\{\mathbf{D}_{t,i}\}_{i=1}^N$ within exposure time. Next, we render each latent sharp image $\hat{\mathbf{I}}_{t,i}$ with the camera pose $\mathbf{P}_{t,i}$, dynamic Gaussians $\mathbf{D}_{t,i}$ and static Gaussians \mathbf{S} . Finally, $\{\hat{\mathbf{I}}_{t,i}\}_{i=1}^N$ are averaged to obtain the synthetic blurry image $\hat{\mathbf{B}}_t$, which is used to calculate the reconstruction loss \mathcal{L}_{rec} with the given blurry frame \mathbf{B}_t . To regularize the under-constrained optimization, we introduce exposure regularization \mathcal{L}_e , multi-frame consistency regularization \mathcal{L}_{mfc} and multi-resolution consistency regularization \mathcal{L}_{mrc} . (b) Rendering of Deblur4DGS. Deblur4DGS produces the sharp image with user-provided timestamp t and camera pose \mathbf{P}_t .

timestamp) and represents the objects by canonical dynamic Gaussians, *i.e.*, \mathbf{C} . Then, \mathbf{C} is deformed to other timestamps for motion representation. Denote by \mathbf{D}_t the dynamic Gaussians at t -th timestamp, it can be written as,

$$\mathbf{D}_t = \mathcal{F}(\mathbf{C}, t; \Theta_{\mathcal{F}}). \quad (1)$$

\mathcal{F} is the deformation operation with parameters $\Theta_{\mathcal{F}}$. The Gaussians for t -th timestamp is the union of \mathbf{S} and \mathbf{D}_t .

Collectively, 4DGS models a scene with static Gaussians \mathbf{S} , canonical dynamic Gaussians \mathbf{C} , and a deformation operation \mathcal{F} . With the provided camera pose, the Gaussians at t -th timestamp \mathbf{D}_t can be projected into 2D spaces and rasterized to obtain the corresponding image.

Motion Blur Formation

Motion blur occurs due to camera shake and object movement, which can be regarded as the integration of latent sharp images (Nah, Hyun Kim, and Mu Lee 2017), *i.e.*,

$$\mathbf{B}(u, v) = \phi \int_0^{\tau} \mathbf{I}_t(u, v) dt. \quad (2)$$

$\mathbf{B} \in \mathbb{R}^{H \times W \times 3}$ is the blurry image and \mathbf{I}_t is the latent sharp one at t -th timestamp. (u, v) is pixel location, τ is the camera exposure time, and ϕ is a normalization factor. To approximate the integral operation, recent works (Zhao, Wang, and Liu 2024; Sun et al. 2024a; Wang et al. 2023) divide the exposure time into N timestamps and regard the blurry image as the average of N sharp images, *i.e.*,

$$\mathbf{B}(u, v) \approx \frac{1}{N} \sum_{i=0}^{N-1} \mathbf{I}_i(u, v). \quad (3)$$

In this work, we reconstruct 4D model from a blurry video by integrating the blur formation into model optimization.

Proposed Method

Let $\{\mathbf{B}_t\}_{t=1}^T$ and $\{\mathbf{M}_t\}_{t=1}^T$ denote a blurry video with T timestamps and the corresponding masks indicating dynamic areas (extracted by SAM2 (Ravi et al. 2024)), respectively. As shown in fig. 1(a), when processing t -th frame, we first evenly divide its camera exposure time into N timestamps. Then, we estimate continuous camera poses $\{\mathbf{P}_{t,i}\}_{i=1}^N$ and dynamic Gaussians $\{\mathbf{D}_{t,i}\}_{i=1}^N$ to simulate camera shake and object movement. Next, we render each sharp image $\hat{\mathbf{I}}_{t,i}$ with the corresponding camera pose $\mathbf{P}_{t,i}$, dynamic Gaussians $\mathbf{D}_{t,i}$ and static Gaussians \mathbf{S} . After that, we average $\{\hat{\mathbf{I}}_{t,i}\}_{i=1}^N$ to obtain the synthetic blurry image $\hat{\mathbf{B}}_t$, which is used to calculate the reconstruction loss \mathcal{L}_{rec} with the given blurry frame \mathbf{B}_t , *i.e.*,

$$\mathcal{L}_{rec} = (1 - \beta) \mathcal{L}_1(\hat{\mathbf{B}}_t, \mathbf{B}_t) + \beta \mathcal{L}_{ssim}(\hat{\mathbf{B}}_t, \mathbf{B}_t). \quad (4)$$

\mathcal{L}_1 and \mathcal{L}_{ssim} are ℓ_1 loss and SSIM (Wang et al. 2004) loss, respectively. β is set to 0.2. The setting all follows 3DGS (Kerbl et al. 2023).

Continuous Camera Poses Estimation

To estimate continuous camera poses, recent methods (Zhao, Wang, and Liu 2024; Peng et al. 2024a; Chen and Liu 2024; Oh et al. 2024) directly optimize exposure start and end poses (*i.e.*, $\mathbf{P}_{t,1}$ and $\mathbf{P}_{t,N}$). Then, the linear interpolation is performed between $\mathbf{P}_{t,1}$ and $\mathbf{P}_{t,N}$ to obtain the camera

pose at i -th intermediate timestamp (*i.e.*, $\mathbf{P}_{t,i}$), *i.e.*,

$$\mathbf{P}_{t,i} = \mathbf{P}_{t,1} \odot \exp\left(\frac{i-1}{N-1} \odot \log\left(\frac{\mathbf{P}_{t,N}}{\mathbf{P}_{t,1}}\right)\right). \quad (5)$$

\exp and \log are exponential and logarithmic functions, respectively. \odot is a pixel-wise multiply operation.

We follow the manner but deploy a tiny MLP as the camera motion predictor (see details in the Sec.A of *Suppl*) for more stable optimization. We pre-train it and static Gaussians \mathbf{S} with static reconstruction loss \mathcal{L}_{rec}^s , *i.e.*,

$$\mathcal{L}_{rec}^s = (1 - \beta)\mathcal{L}_1(\hat{\mathbf{B}}_t^s, \mathbf{B}_t^s) + \beta\mathcal{L}_{ssim}(\hat{\mathbf{B}}_t^s, \mathbf{B}_t^s). \quad (6)$$

$\hat{\mathbf{B}}_t^s = (1 - \mathbf{M}_t) \odot \hat{\mathbf{B}}_t$ and $\mathbf{B}_t^s = (1 - \mathbf{M}_t) \odot \mathbf{B}_t$ are the static areas of $\hat{\mathbf{B}}_t$ and \mathbf{B}_t , respectively.

Continuous Dynamic Gaussians Estimation

We first introduce blur-aware variable canonical Gaussians for better dynamic representation at integer timestamps. Then, we describe Gaussian deformation manner. Finally, we detail how to take learnable exposure time parameters to obtain continuous dynamic Gaussians within exposure time. **Blur-Aware Variable Canonical Gaussians.** Existing 4D reconstruction methods generally select a single canonical Gaussians \mathbf{C} across the entire video, which may produce results with missing details in scenes with large motion. To alleviate the issue, we suggest varying the canonical Gaussians as time progresses. In such case, the k -th canonical Gaussians \mathbf{C}_k is only used for some nearby timestamps, thus reducing the difficulty of motion modeling. One way to achieve this is to uniformly divide the video into L segments and select \mathbf{C}_k for k -th segment. Although it improves performance, selecting the one corresponding to the sharper frame is better for blur removal. In particular, we first uniformly divide the video into L segments and calculate the blur level b_t of dynamic areas for t -th frame following (Bansal, Raj, and Choudhury 2016; Ren, Qian, and Chen 2020), *i.e.*,

$$b_t = \sum_{(u,v) \in \mathbf{M}_t} (\Delta \mathbf{B}_t(u,v) - \overline{\Delta \mathbf{B}_t})^2. \quad (7)$$

\mathbf{M}_t indicates dynamic areas. $\Delta \mathbf{B}_t$ is the image Laplacian and $\overline{\Delta \mathbf{B}_t}$ is its mean value. The larger b_t is, the sharper the frame is. To make the start and end frame of the segment as sharp as possible, we look for the sharp frame among their surrounding H frames and redefine them as the start and end of current segment. Finally, we select the Gaussians for the sharpest frame in each segment as its canonical ones.

Gaussian Deformation. We deform dynamic Gaussians with a set of rigid transformation matrices, following Shape-of-Motion (Wang et al. 2024). Let $\{\mathbf{x}_c, \mathbf{r}_c, \mathbf{s}, \mathbf{o}, \mathbf{c}\}$, $\{\mathbf{x}_t, \mathbf{r}_t, \mathbf{s}, \mathbf{o}, \mathbf{c}\}$, and $\{\mathbf{A}_t, \mathbf{E}_t\}$ denote a Gaussian in \mathbf{C}_k , the ones in \mathbf{D}_t , and the corresponding transformation matrix, respectively. It can be written as,

$$\mathbf{x}_t = \mathbf{A}_t \mathbf{x}_c + \mathbf{E}_t, \quad \mathbf{r}_t = \mathbf{A}_t \mathbf{r}_c. \quad (8)$$

Interpolation with Exposure Time Parameters. To get continuous dynamic Gaussians $\{\mathbf{D}_{t,i}\}_{i=1}^N$, one straightforward way is to deploy a series of learnable Gaussian or deformation parameters, but it is unstable to optimize. With the

explicit object motion representation in eq. (8), $\mathbf{D}_{t,i}$ can be calculated by interpolating between the ones at the nearest integer timestamps, *i.e.*,

$$\begin{aligned} \mathbf{D}_{t,i} &= \mathbf{w}_{t,i} \odot \mathbf{D}_{t-1} + (1 - \mathbf{w}_{t,i}) \odot \mathbf{D}_t, \quad i \in [1, N/2], \\ \mathbf{D}_{t,i} &= (1 - \mathbf{w}_{t,i}) \odot \mathbf{D}_t + \mathbf{w}_{t,i} \odot \mathbf{D}_{t+1}, \quad i \in [N/2, N]. \end{aligned} \quad (9)$$

$\mathbf{w}_{t,i}$ is the normalized time interval between $\mathbf{D}_{t,i}$ and $\mathbf{D}_{t,N/2}$. Thus, the problem is transformed to estimate $\mathbf{w}_{t,i}$. In the implementation, we can estimate the one at exposure start and end (*i.e.*, $\mathbf{w}_{t,1}$ and $\mathbf{w}_{t,N}$) and then interpolate between them to get the i -th intermediate one $\mathbf{w}_{t,i}$, *i.e.*,

$$\mathbf{w}_{t,i} = \left(1 - \frac{i-1}{N-1}\right) \odot \mathbf{w}_{t,1} + \frac{i-1}{N-1} \odot \mathbf{w}_{t,N}. \quad (10)$$

As the object motion within the exposure can be regarded as uniform, the absolute value of $\mathbf{w}_{t,1}$ and $\mathbf{w}_{t,N}$ are equal, which is half the exposure time \mathbf{w}_t . Thus, eq. (10) can be re-written as,

$$\mathbf{w}_{t,i} = \left(1 - \frac{i-1}{N-1}\right) \odot \frac{\mathbf{w}_t}{2} + \frac{i-1}{N-1} \odot \left(-\frac{\mathbf{w}_t}{2}\right). \quad (11)$$

Finally, we set learnable parameters \mathbf{w}_t for continuous dynamic Gaussians estimation within the exposure time. The canonical Gaussians, Gaussian deformation modules, and \mathbf{w}_t are jointly optimized. The reconstruction loss for dynamic areas is similar to eq. (6).

Regularization Terms

After optimization with eq. (4), static areas of $\hat{\mathbf{I}}_{t,i}$ are sharp while dynamic areas can with notable artifacts. The reasons are below. (1) Note that multiple solutions exist for the model to fulfill eq. (4). The most ideal one is that every $\hat{\mathbf{I}}_{t,i}$ is sharp, and the most trivial one is that every $\hat{\mathbf{I}}_{t,i}$ is as blurry as \mathbf{B}_t . (2) As static areas are consistent across the entire video, the model tends to learn the underlying sharp representation for inter-frame consistency. In other words, the inter-frame consistency implicitly regularizes model optimization. To further validate this, we conduct an experiment that removes the inter-frame consistency by reducing the number of frames to one. In such a case, the static areas are blurry after optimization with eq. (4), which supports our confirmation. (3) Compared to static areas, the inter-frame consistency in dynamic ones is weaker due to object motion. It may provide insufficient regularization to guide sharp representation learning, thus leading to artifacts. To avoid this, we introduce regularization terms \mathcal{L}_{reg} , including exposure regularization \mathcal{L}_e , multi-frame consistency term \mathcal{L}_{mfc} , and multi-resolution consistency term \mathcal{L}_{mrc} .

First, the continuous dynamic Gaussians $\{\mathbf{D}_{t,i}\}_{i=1}^N$ should not be the same. In other words, the value of exposure time parameters \mathbf{w}_t should not be too small. If \mathbf{w}_t is too small, $\mathbf{D}_{t,i}$ is nearly the same as \mathbf{D}_t , leading to trivial solutions. We constrain \mathbf{w}_t by \mathcal{L}_e , as,

$$\mathcal{L}_e = \max(0, \epsilon - \mathbf{w}_t). \quad (12)$$

\max is the maximum function and ϵ is a threshold.

Second, despite different motions, the content of multiple frames within exposure time should be similar. We utilize

Table 1: novel view synthesis results on synthetic videos.

Methods	PSNR↑/SSIM↑/LPIPS↓ 288 × 512	PSNR↑/SSIM↑/LPIPS↓ 720 × 1080
DeformableGS	15.73 / 0.623 / 0.382	15.55 / 0.667 / 0.421
4DGaussians	21.98 / 0.801 / 0.197	21.69 / 0.831 / 0.264
E-D3DGS	23.09 / 0.830 / 0.175	22.46 / 0.844 / 0.258
Shape-of-Motion	26.06 / 0.910 / 0.144	25.81 / 0.897 / 0.246
SplineGS	26.05 / 0.901 / 0.158	24.92 / 0.883 / 0.252
DyBluRF	26.04 / 0.916 / 0.090	25.71 / 0.908 / 0.159
BARD-GS	26.91 / 0.923 / 0.077	26.34 / 0.909 / 0.139
Deblur4DGS (Ours)	27.66 / 0.935 / 0.060	27.16 / 0.927 / 0.123

\mathcal{L}_{fc} to constrain consistency between neighbor frames, and that between each frame and the first frame, *i.e.*,

$$\mathcal{L}_{mfc} = \frac{1}{N-1} \sum_{i=2}^N \left(\left\| \mathbf{M}_{t,i} \odot (\hat{\mathbf{I}}_{t,i-1 \rightarrow i} - \hat{\mathbf{I}}_{t,i}) \right\|_1 + \left\| \mathbf{M}_{t,1} \odot (\hat{\mathbf{I}}_{t,i \rightarrow 1} - \hat{\mathbf{I}}_{t,1}) \right\|_1 \right). \quad (13)$$

$\hat{\mathbf{I}}_{t,i-1 \rightarrow i}$ and $\hat{\mathbf{I}}_{t,i \rightarrow 1}$ are obtained by aligning $\hat{\mathbf{I}}_{t,i-1}$ to $\hat{\mathbf{I}}_{t,i}$ and aligning $\hat{\mathbf{I}}_{t,i}$ to $\hat{\mathbf{I}}_{t,1}$ with a pre-trained optical flow network (Sun et al. 2018), respectively. $\mathbf{M}_{t,i}$ and $\mathbf{M}_{t,1}$ are dynamic masks for $\hat{\mathbf{I}}_{t,i}$ and $\hat{\mathbf{I}}_{t,1}$, respectively.

Third, the blur in the lower resolution is lower level and is easier to remove (Kim, Lee, and Cho 2022; Tao et al. 2018), thus the artifacts are less in models trained with down-sampled blurry video. Taking this advantage, we impose \mathcal{L}_{mrc} to assist the optimization of high-resolution models with results from low-resolution models, *i.e.*,

$$\mathcal{L}_{mrc} = \|(\mathbf{M}_{t,i})_{\downarrow} \odot ((\hat{\mathbf{I}}_{t,i})_{\downarrow} - \text{sg}(\hat{\mathbf{I}}_{t,i}^l))\|_1. \quad (14)$$

$\hat{\mathbf{I}}_{t,i}^l$ is the rendered sharp image from the low-resolution model, which is pre-trained by taking the down-sampled video as supervision. $(\cdot)_{\downarrow}$ is an image down-sampling operation. sg is the stop-gradient operation.

Overall, regularization terms \mathcal{L}_{reg} can be denoted as,

$$\mathcal{L}_{reg} = \lambda_e \mathcal{L}_e + \lambda_{mfc} \mathcal{L}_{mfc} + \lambda_{mrc} \mathcal{L}_{mrc}. \quad (15)$$

λ_e , λ_{mfc} , and λ_{mrc} are set to 0.1, 2, 1, respectively. Besides, following Shape-of-Motion (Wang et al. 2024), we also use some other regularization terms \mathcal{L}_{oth} to help reconstruct 3D motion better, and the details are in the Sec.B of *Suppl.*

Application to Multiple Tasks

The blurry videos suffer from not only motion blur, but also low frame rates and scene shake generally. Beyond novel-view synthesis, Deblur4DGS can adjust the camera poses and timestamps to address these problems, achieving video deblurring, frame interpolation, and video stabilization. First, when inputting camera poses of the blurry video, Deblur4DGS can render corresponding deblurring results. Second, when feeding the interpolated camera poses and timestamps, Deblur4DGS can produce frame-interpolated results. Third, Deblur4DGS can render a more stable video with the smoothed camera poses as inputs.

Table 2: novel view synthesis results on real-world videos.

Methods	CLIPQA↑/MUSIQ↑ Redmi	PSNR↑/SSIM↑/LPIPS↓ BARD-GS
DeformableGS	0.238 / 25.903	15.63 / 0.781 / 0.361
4DGaussians	0.236 / 26.514	21.32 / 0.863 / 0.221
E-D3DGS	0.257 / 24.967	22.69 / 0.883 / 0.217
Shape-of-Motion	0.277 / 24.538	20.53 / 0.854 / 0.289
SplineGS	0.252 / 32.022	23.93 / 0.899 / 0.197
DyBluRF	0.263 / 34.006	22.71 / 0.878 / 0.192
BARD-GS	0.288 / 35.505	22.69 / 0.874 / 0.177
Deblur4DGS (Ours)	0.356 / 36.756	23.10 / 0.879 / 0.161

Experiments

Experimental Settings

Training Details. For stable optimization, we pre-train the camera motion predictor and static Gaussians \mathbf{S} for 400 epochs. After that, we jointly optimize the camera motion predictor, \mathbf{S} , canonical dynamic Gaussians $\{\mathbf{C}_k\}_{k=1}^K$, deformable operation \mathcal{F} and exposure time parameters $\{\mathbf{w}_t\}_{t=1}^T$ for 200 epochs. The learning rate for camera motion predictor is set to 5×10^{-4} and decayed to 1×10^{-5} . The learning rate for $\{\mathbf{w}_t\}_{t=1}^T$ is set to 1×10^{-1} and decayed to 1×10^{-5} . The learning rate for \mathbf{S} , $\{\mathbf{C}_k\}_{k=1}^K$ and \mathcal{F} follows Shape-of-Motion (Wang et al. 2024). N is set to 11. L and H are set to 5 and 3 respectively. ϵ is set to 1.0. All experiments are conducted with PyTorch (Paszke et al. 2019) on one Nvidia GeForce RTX A6000 GPU.

Evaluation Configurations. The synthetic data contains 9 scenes with significant motion blur from Stereo Blur Dataset (Zhou et al. 2019), where each scene contains blurry stereo videos and the corresponding sharp ones. Note that DyBluRF (Sun et al. 2024a) conducts experiments on $\times 2.5$ down-sampled data. We evaluate on both $\times 2.5$ down-sampled ones (*i.e.*, 288×512) and the original ones (*i.e.*, 720×1080). For novel-view synthesis and deblurring, the rendering results may be spatially misaligned with ground truth due to the calibration error of camera parameters. Thus, we first freeze the pre-trained 4D model and optimize camera poses by minimizing the photometric error between rendering results and ground truth, and then calculate metrics (*i.e.*, PSNR (Huynh-Thu and Ghanbari 2008), SSIM (Wang et al. 2004) and LPIPS (Zhang et al. 2018b)), following COLMAP-Free 3DGS (Fu et al. 2024). As there is no ground truth for frame interpolation and video stabilization, we employ recent no-reference metrics, *i.e.*, CLIPQA (Wang, Chan, and Loy 2023) and MUSIQ (Ke et al. 2021). Besides, we evaluate on 6 real-world blurry videos (*i.e.*, Redmi data) captured by a Redmi K50 Ultra smartphone and 12 real-world ones (*i.e.*, BARD-GS data) from BARD-GS (Lu et al. 2025), where each one contains 24 frames. For novel-view synthesis, we employ no-reference metrics (*i.e.*, CLIPQA and MUSIQ) and full-reference metrics (*i.e.*, PSNR, SSIM and LPIPS) for the two data, respectively. For the other three tasks, we use no-reference metrics (*i.e.*, CLIPQA and MUSIQ) due to no ground truth.



Figure 2: Visual comparisons of novel-view synthesis on real-world videos. Our method produces more photo-realistic details and less visual artifacts in both static and dynamic areas, as marked with yellow and red boxes respectively.

Table 3: Results that pre-process the blurry video with an image or video deblurring method before 4D reconstruction. ‘None’ denotes no deblurring method being used.

4D Methods	Deblurring Methods	PSNR \uparrow / SSIM \uparrow / LPIPS \downarrow 288 \times 512	PSNR \uparrow / SSIM \uparrow / LPIPS \downarrow 720 \times 1080
E-D3DGS	None	23.09 / 0.830 / 0.175	22.46 / 0.844 / 0.258
	Restormer	23.79 / 0.850 / 0.142	22.87 / <u>0.864</u> / 0.198
	DSTNet	23.59 / 0.861 / <u>0.132</u>	<u>22.93</u> / 0.863 / <u>0.188</u>
	BSSTNet	<u>23.68</u> / <u>0.855</u> / 0.128	23.20 / 0.877 / 0.176
Shape-of-Motion	None	26.06 / 0.910 / 0.144	25.81 / 0.897 / 0.246
	Restormer	26.80 / 0.917 / 0.085	26.20 / 0.911 / 0.169
	DSTNet	26.60 / 0.915 / <u>0.082</u>	<u>26.08</u> / <u>0.914</u> / <u>0.140</u>
	BSSTNet	<u>26.78</u> / <u>0.916</u> / 0.080	26.06 / 0.916 / 0.125
Deblur4DGS	None	27.66 / 0.935 / 0.060	27.16 / 0.927 / 0.123

Comparison with State-of-the-Art Methods

We compare with 7 state-of-the-art methods (*i.e.*, DeformableGS (Yang et al. 2024), 4DGaussians (Wu et al. 2024), E-D3DGS (Bae et al. 2024), Shape-of-Motion (Wang et al. 2024), SplineGS (Park et al. 2025), DyBluRF (Sun et al. 2024a) and BARD-GS (Lu et al. 2025)), where DyBluRF and BARD-GS are designed for 4D reconstruction from blurry monocular video based on NeRF (Mildenhall et al. 2021) and 3DGS (Kerbl et al. 2023) respectively.

Novel-view synthesis. table 1 and table 2 summarize the results. First, methods (*i.e.*, DyBluRF and BARD-GS) that perform 4D reconstruction and motion blur modeling jointly yield overall better performance, especially in LPIPS score. Although SplineGS (Park et al. 2025) gets better PSNR and SSIM scores in BARD-GS data, it produces blurry outputs. It is consistent with the finding in BARD-GS (Wang et al. 2024) that PSNR can sometimes yield higher values even when images appear blurrier. Second, benefiting the explicit 3D representation manner, BARD-GS outperforms DyBluRF, being the most competitive method. Third, compared with BARD-GS, our Deblur4DGS performs better due to the introduction of a series of regularization terms to avoid trivial solutions and blur-aware variable canonical Gaussians to better represent dynamic objects. Visual results in fig. 9

shows that Deblur4DGS removes blur more clearly and produces less visual artifacts in both static and dynamic areas. Per-scene results, more visual results and rendering speed comparisons are in the Sec.C of *Suppl.*

In addition, to further demonstrate the effectiveness of Deblur4DGS, we first pre-process the blurry videos with state-of-the-art image (*i.e.*, Restormer (Zamir et al. 2022)) or video (DSTNet (Pan et al. 2023) and BSSTNet (Zhang, Xie, and Yao 2024)) deblurring methods and then perform 4D reconstruction, as shown in table 3. Compared with reconstruction from blurry videos, the incorporation of deblurring models improves performance. This is because the deblurring models remove some blur, facilitating sharp scene reconstruction. However, as the deblurring methods cannot perceive 3D structure and maintain scene geometric consistency, the reconstruction results are still unsatisfactory. In contrast, Deblur4DGS jointly reconstructs scene geometry and processes motion blur in 3D space, achieving better scene reconstruction results.

Deblurring. Apart from 4D reconstruction-based methods, we compare with some state-of-the-art image and video deblurring ones. The results are in the Sec.C of *Suppl.* Deblur4DGS obtains better results than 4D reconstruction-based methods and comparable ones to deblurring-specific ones. Compared with the former, Deblur4DGS better reconstructs the scene, thus performing better. Note that the latter ones are trained on large paired data in supervised manner while Deblur4DGS is optimized with the given blurry video in a self-supervised manner. Although the data prior makes them perform better, Deblur4DGS is more convenient to use.

Frame Interpolation. We interpolate camera poses and timestamps to generate $\times 16$ frame interpolation results. We compare with 4D reconstruction-based methods and some video frame interpolation ones (*i.e.*, RIFE (Huang et al. 2022), EMAVFI (Zhang et al. 2023a), and VIDUE (Shang et al. 2023)). The results are in the Sec.C of *Suppl.* VIDUE is trained with large paired data in a supervised manner for joint deblurring and frame interpolation, thus achieving bet-

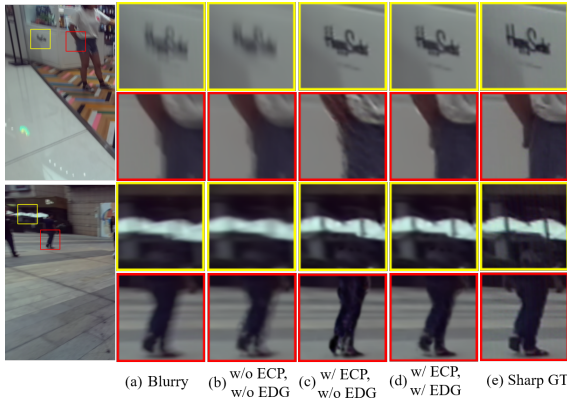


Figure 3: Effect of continuous camera pose (ECP) and dynamic Gaussian (EDG) estimation.

ter results. Deform4DGS performs satisfactorily overall.

Video Stabilization. We employ a Gaussian filter to smooth camera poses for video stabilization, following (Peng et al. 2024b). The results are in the Sec.C of *Suppl.* Deblur4DGS achieves pleasant scores compared with 2D video stabilization methods (*i.e.*, MeshFlow (Liu et al. 2016) and NNDVS (Zhang et al. 2023b)) and 4D reconstruction-based ones, which benefits from better geometry reconstruction.

Ablation Study

We conduct experiments to validate the effectiveness of each strategy. As our strategies in Deblur4DGS are mainly designed to process dynamic areas, we exclude the pixels of static areas to calculate the metrics in dynamic ones.

Effect of ECP and EDG

ECP and EDG are introduced to process camera motion blur and object motion blur, respectively. Quantitative results and visual comparisons are shown in table 4 and fig. 3, respectively. First, without ECP and EDG, the results are almost as blurry as the input frame, as shown in fig. 3(b). Second, only with ECP, the static areas are sharp but may lead to visual artifacts in dynamic areas, as shown in fig. 3(c). It is because ECP cannot simulate the object movement. Third, we further introduce EDG to simulate that, producing visually pleasant results in both areas, as shown in fig. 3(d).

Effect of Regularization Terms

The effect of exposure regularization \mathcal{L}_e , multi-frame consistency term \mathcal{L}_{mfc} and multi-resolution consistency term \mathcal{L}_{mrc} are in table 5. Visual results are in the Sec.D of *Suppl.* Without these regularization terms, noticeable artifacts appear in dynamic regions, resulting in degraded performance. By regularizing the object motion within the exposure time distinguished, \mathcal{L}_e improves performance. Besides, \mathcal{L}_{mfc} and \mathcal{L}_{mrc} additionally regularize multi-frame and multi-resolution consistency respectively, helping to alleviate artifacts. Their combinations perform best.

Table 4: Effect about the estimation of continuous camera poses (ECP) and dynamic Gaussians (EDG).

ECP	EDG	PSNR \uparrow /SSIM \uparrow /LPIPS \downarrow 288 \times 512	PSNR \uparrow /SSIM \uparrow /LPIPS \downarrow 720 \times 1080
\times	\times	22.10 / 0.988 / 0.018	22.34 / 0.988 / 0.016
\checkmark	\times	22.30 / 0.989 / 0.016	22.39 / 0.988 / 0.015
\checkmark	\checkmark	22.36 / 0.989 / 0.015	22.63 / 0.990 / 0.014

Table 5: Effect of regularization terms (see eq. (15)).

\mathcal{L}_e	\mathcal{L}_{mfc}	\mathcal{L}_{mrc}	PSNR \uparrow /SSIM \uparrow /LPIPS \downarrow 288 \times 512	PSNR \uparrow /SSIM \uparrow /LPIPS \downarrow 720 \times 1080
\times	\times	\times	21.87 / 0.987 / 0.017	22.30 / 0.988 / 0.016
\times	\checkmark	\checkmark	22.30 / 0.989 / 0.015	22.56 / 0.989 / 0.015
\checkmark	\times	\times	22.01 / 0.988 / 0.015	22.40 / 0.989 / 0.015
\checkmark	\checkmark	\times	22.16 / 0.989 / 0.016	22.49 / 0.989 / 0.015
\checkmark	\times	\checkmark	22.22 / 0.989 / 0.015	22.54 / 0.989 / 0.014
\checkmark	\checkmark	\checkmark	22.36 / 0.989 / 0.015	22.63 / 0.990 / 0.014

Table 6: Effect of blur-aware variable (BAV) canonical Gaussians. ‘None’ denotes selecting a single one.

Methods	PSNR \uparrow /SSIM \uparrow /LPIPS \downarrow 288 \times 512	PSNR \uparrow /SSIM \uparrow /LPIPS \downarrow 720 \times 1080
None	22.13 / 0.988 / 0.017	22.30 / 0.988 / 0.016
w/o Blur-Aware	22.29 / 0.989 / 0.016	22.57 / 0.989 / 0.015
Ours	22.36 / 0.989 / 0.015	22.63 / 0.990 / 0.014

Effect of BAV Canonical Gaussians.

The results are summarized in table 6. First, selecting a single canonical Gaussians across the entire video (*i.e.*, None) leads to poor performance, due to the challenge of modeling large object motion. Second, selecting variable canonical Gaussians uniformly (*i.e.*, w/o Blur-Aware) alleviates this, leading to performance gain. We also experiment with an optical flow-based strategy (Shaw et al.) to select canonical Gaussians, performs similar to the uniform selection. This may be due to the inaccurate estimation of optical flow from blurry images. Third, our blur-aware selection is better, as the canonical Gaussians corresponding to the sharper frame help blur removal. Visual results are in the Sec.D of *Suppl.*

Conclusions

In this work, we propose Deblur4DGS, a 4D Gaussian Splatting framework to reconstruct a high-quality 4D model from blurry monocular video. In particular, with the explicit motion trajectory modeling, we propose to transform the challenging continuous dynamic representation estimation within an exposure time into the exposure time estimation, where a series of regularizations are suggested to tackle the under-constrained optimization. Besides, a blur-aware variable canonical Gaussians is present to represent objects with large motion better. Beyond novel-view synthesis, Deblur4DGS can improve blurry video quality from multiple perspectives, including deblurring, frame interpolation, and video stabilization. Extensive results show Deblur4DGS outperforms state-of-the-art 4D reconstruction methods.

References

- Bae, J.; Kim, S.; Yun, Y.; Lee, H.; Bang, G.; and Uh, Y. 2024. Per-Gaussian Embedding-Based Deformation for Deformable 3D Gaussian Splatting. *arXiv*.
- Bansal, R.; Raj, G.; and Choudhury, T. 2016. Blur image detection using Laplacian operator and Open-CV. In *SMART*, 63–67. IEEE.
- Bui, M.-Q. V.; Park, J.; Oh, J.; and Kim, M. 2023. Dyblurf: Dynamic deblurring neural radiance fields for blurry monocular video. *arXiv*.
- Cao, A.; and Johnson, J. 2023. Hexplane: A fast representation for dynamic scenes. In *CVPR*, 130–141.
- Chan, K. C.; Zhou, S.; Xu, X.; and Loy, C. C. 2022. BasicVSR++: Improving video super-resolution with enhanced propagation and alignment. In *CVPR*, 5972–5981.
- Chen, W.; and Liu, L. 2024. Deblur-GS: 3D Gaussian Splatting from Camera Motion Blurred Images. *ACM*, 7(1): 1–15.
- Chu, W.-H.; Ke, L.; and Fragkiadaki, K. 2024. Dreamscene4d: Dynamic multi-object scene generation from monocular videos. *arXiv*.
- Doersch, C.; Yang, Y.; Vecerik, M.; Gokay, D.; Gupta, A.; Aytaç, Y.; Carreira, J.; and Zisserman, A. 2023. Tapir: Tracking any point with per-frame initialization and temporal refinement. In *ICCV*, 10061–10072.
- Duan, Y.; Wei, F.; Dai, Q.; He, Y.; Chen, W.; and Chen, B. 2024a. 4d gaussian splatting: Towards efficient novel view synthesis for dynamic scenes. *arXiv*.
- Duan, Y.; Wei, F.; Dai, Q.; He, Y.; Chen, W.; and Chen, B. 2024b. 4d-rotor gaussian splatting: towards efficient novel view synthesis for dynamic scenes. In *SIGGRAPH*, 1–11.
- Fu, Y.; Liu, S.; Kulkarni, A.; Kautz, J.; Efros, A. A.; and Wang, X. 2024. COLMAP-Free 3D Gaussian Splatting. In *CVPR*, 20796–20805.
- Gao, Q.; Xu, Q.; Cao, Z.; Mildenhall, B.; Ma, W.; Chen, L.; Tang, D.; and Neumann, U. 2024. Gaussianflow: Splatting gaussian dynamics for 4d content creation. *arXiv*.
- Huang, Y.-H.; Sun, Y.-T.; Yang, Z.; Lyu, X.; Cao, Y.-P.; and Qi, X. 2024. Sc-gs: Sparse-controlled gaussian splatting for editable dynamic scenes. In *CVPR*, 4220–4230.
- Huang, Z.; Zhang, T.; Heng, W.; Shi, B.; and Zhou, S. 2022. Real-time intermediate flow estimation for video frame interpolation. In *ECCV*, 624–642. Springer.
- Huynh-Thu, Q.; and Ghanbari, M. 2008. Scope of validity of PSNR in image/video quality assessment. *Electronics letters*, 44(13): 800–801.
- Katsumata, K.; Vo, D. M.; and Nakayama, H. 2024. A Compact Dynamic 3D Gaussian Representation for Real-Time Dynamic View Synthesis. In *ECCV*.
- Ke, J.; Wang, Q.; Wang, Y.; Milanfar, P.; and Yang, F. 2021. Musiq: Multi-scale image quality transformer. In *ICCV*, 5148–5157.
- Kerbl, B.; Kopanas, G.; Leimkühler, T.; and Drettakis, G. 2023. 3D Gaussian Splatting for Real-Time Radiance Field Rendering. *ACM*, 42(4): 139–1.
- Kim, K.; Lee, S.; and Cho, S. 2022. Mssnet: Multi-scale-stage network for single image deblurring. In *ECCV*, 524–539. Springer.
- Kong, L.; Dong, J.; Ge, J.; Li, M.; and Pan, J. 2023. Efficient frequency domain-based transformers for high-quality image deblurring. In *CVPR*, 5886–5895.
- Kratimenos, A.; Lei, J.; and Daniilidis, K. 2023. Dynmf: Neural motion factorization for real-time dynamic view synthesis with 3d gaussian splatting. *arXiv*.
- Lee, B.; Lee, H.; Sun, X.; Ali, U.; and Park, E. 2024a. Deblurring 3d gaussian splatting. *arXiv*.
- Lee, D.; Lee, M.; Shin, C.; and Lee, S. 2023a. Dp-nerf: Deblurred neural radiance field with physical scene priors. In *CVPR*, 12386–12396.
- Lee, D.; Oh, J.; Rim, J.; Cho, S.; and Lee, K. M. 2023b. Exblurf: Efficient radiance fields for extreme motion blurred images. In *ICCV*, 17639–17648.
- Lee, J.; Kim, D.; Lee, D.; Cho, S.; and Lee, S. 2024b. CRiM-GS: Continuous Rigid Motion-Aware Gaussian Splatting from Motion Blur Images. *arXiv*.
- Lee, Y.-C.; Zhang, Z.; Blackburn-Matzen, K.; Niklaus, S.; Zhang, J.; Huang, J.-B.; and Liu, F. 2023c. Fast view synthesis of casual videos. *arXiv*.
- Lei, J.; Weng, Y.; Harley, A.; Guibas, L.; and Daniilidis, K. 2024. MoSca: Dynamic Gaussian Fusion from Casual Videos via 4D Motion Scaffolds. *arXiv*.
- Li, J.; Wang, W.; Nan, Y.; and Ji, H. 2023. Self-supervised blind motion deblurring with deep expectation maximization. In *CVPR*, 13986–13996.
- Li, Z.; Chen, Z.; Li, Z.; and Xu, Y. 2024. Spacetime gaussian feature splatting for real-time dynamic view synthesis. In *CVPR*, 8508–8520.
- Liang, J.; Cao, J.; Fan, Y.; Zhang, K.; Ranjan, R.; Li, Y.; Timofte, R.; and Van Gool, L. 2024. Vrt: A video restoration transformer. *TIP*.
- Lin, J.; Zhang, Z.; Wei, Y.; Ren, D.; Jiang, D.; Tian, Q.; and Zuo, W. 2024a. Improving image restoration through removing degradations in textual representations. In *CVPR*, 2866–2878.
- Lin, Y.; Dai, Z.; Zhu, S.; and Yao, Y. 2024b. Gaussianflow: 4d reconstruction with dynamic 3d gaussian particle. In *CVPR*, 21136–21145.
- Liu, S.; Tan, P.; Yuan, L.; Sun, J.; and Zeng, B. 2016. Meshflow: Minimum latency online video stabilization. In *ECCV*, 800–815. Springer.
- Lu, Y.; Zhou, Y.; Liu, D.; Liang, T.; and Yin, Y. 2025. Bardgs: Blur-aware reconstruction of dynamic scenes via gaussian splatting. In *CVPR*, 16532–16542.
- Lu, Z.; Guo, X.; Hui, L.; Chen, T.; Yang, M.; Tang, X.; Zhu, F.; and Dai, Y. 2024. 3d geometry-aware deformable gaussian splatting for dynamic view synthesis. In *CVPR*, 8900–8910.
- Luiten, J.; Kopanas, G.; Leibe, B.; and Ramanan, D. 2023. Dynamic 3d gaussians: Tracking by persistent dynamic view synthesis. *arXiv*.

- Ma, L.; Li, X.; Liao, J.; Zhang, Q.; Wang, X.; Wang, J.; and Sander, P. V. 2022. Deblur-nerf: Neural radiance fields from blurry images. In *CVPR*, 12861–12870.
- Mihajlovic, M.; Prokudin, S.; Tang, S.; Maier, R.; Bogo, F.; Tung, T.; and Boyer, E. 2024. SplatFields: Neural Gaussian Splats for Sparse 3D and 4D Reconstruction. *arXiv*.
- Mildenhall, B.; Srinivasan, P. P.; Tancik, M.; Barron, J. T.; Ramamoorthi, R.; and Ng, R. 2021. Nerf: Representing scenes as neural radiance fields for view synthesis. *ACM*, 65(1): 99–106.
- Nah, S.; Hyun Kim, T.; and Mu Lee, K. 2017. Deep multi-scale convolutional neural network for dynamic scene deblurring. In *CVPR*, 3883–3891.
- Oh, J.; Chung, J.; Lee, D.; and Lee, K. M. 2024. DeblurGS: Gaussian Splatting for Camera Motion Blur. *arXiv*.
- Pan, J.; Xu, B.; Dong, J.; Ge, J.; and Tang, J. 2023. Deep Discriminative Spatial and Temporal Network for Efficient Video Deblurring. In *CVPR*.
- Park, J.; Bui, M.-Q. V.; Bello, J. L. G.; Moon, J.; Oh, J.; and Kim, M. 2025. Splines: Robust motion-adaptive spline for real-time dynamic 3d gaussians from monocular video. In *CVPR*, 26866–26875.
- Paszke, A.; Gross, S.; Massa, F.; Lerer, A.; Bradbury, J.; Chanan, G.; Killeen, T.; Lin, Z.; Gimelshein, N.; Antiga, L.; et al. 2019. Pytorch: An imperative style, high-performance deep learning library. *NeurIPS*, 32.
- Peng, C.; Tang, Y.; Zhou, Y.; Wang, N.; Liu, X.; Li, D.; and Chellappa, R. 2024a. BAGS: Blur Agnostic Gaussian Splatting through Multi-Scale Kernel Modeling. *arXiv*.
- Peng, Z.; Ye, X.; Zhao, W.; Liu, T.; Sun, H.; Li, B.; and Cao, Z. 2024b. 3D Multi-frame Fusion for Video Stabilization. In *CVPR*, 7507–7516.
- Ravi, N.; Gabeur, V.; Hu, Y.-T.; Hu, R.; Ryali, C.; Ma, T.; Khedr, H.; Rädle, R.; Rolland, C.; Gustafson, L.; Mintun, E.; Pan, J.; Alwala, K. V.; Carion, N.; Wu, C.-Y.; Girshick, R.; Dollár, P.; and Feichtenhofer, C. 2024. SAM 2: Segment Anything in Images and Videos. *arXiv*.
- Ren, M.; Delbracio, M.; Talebi, H.; Gerig, G.; and Milanfar, P. 2023. Multiscale structure guided diffusion for image deblurring. In *ICCV*, 10721–10733.
- Ren, X.; Qian, Z.; and Chen, Q. 2020. Video deblurring by fitting to test data. *arXiv*.
- Seidenschwarz, J.; Zhou, Q.; Duisterhof, B.; Ramanan, D.; and Leal-Taixé, L. 2024. DynOMo: Online Point Tracking by Dynamic Online Monocular Gaussian Reconstruction. *arXiv*.
- Shang, W.; Ren, D.; Yang, Y.; Zhang, H.; Ma, K.; and Zuo, W. 2023. Joint Video Multi-Frame Interpolation and Deblurring under Unknown Exposure Time. In *CVPR*, 13935–13944.
- Shaw, R.; Nazarczuk, M.; Song, J.; Moreau, A.; Catley-Chandar, S.; Dharmo, H.; and Pérez-Pellitero, E. ??? SWinGS: Sliding Windows for Dynamic 3D Gaussian Splatting.
- Somraj, N.; Choudhary, K.; Mupparaju, S. H.; and Soundararajan, R. 2024. Factorized Motion Fields for Fast Sparse Input Dynamic View Synthesis. In *SIGGRAPH*, 1–12.
- Sun, D.; Yang, X.; Liu, M.-Y.; and Kautz, J. 2018. Pw-net: Cnns for optical flow using pyramid, warping, and cost volume. In *CVPR*, 8934–8943.
- Sun, H.; Li, X.; Shen, L.; Ye, X.; Xian, K.; and Cao, Z. 2024a. DyBluRF: Dynamic Neural Radiance Fields from Blurry Monocular Video. In *CVPR*, 7517–7527.
- Sun, J.; Jiao, H.; Li, G.; Zhang, Z.; Zhao, L.; and Xing, W. 2024b. 3dstream: On-the-fly training of 3d gaussians for efficient streaming of photo-realistic free-viewpoint videos. In *CVPR*, 20675–20685.
- Tao, X.; Gao, H.; Shen, X.; Wang, J.; and Jia, J. 2018. Scale-recurrent network for deep image deblurring. In *CVPR*, 8174–8182.
- Tian, F.; Du, S.; and Duan, Y. 2023. Mononerf: Learning a generalizable dynamic radiance field from monocular videos. In *ICCV*, 17903–17913.
- Wang, J.; Chan, K. C.; and Loy, C. C. 2023. Exploring clip for assessing the look and feel of images. In *AAAI*, volume 37, 2555–2563.
- Wang, P.; Zhao, L.; Ma, R.; and Liu, P. 2023. Bad-nerf: Bundle adjusted deblur neural radiance fields. In *CVPR*, 4170–4179.
- Wang, Q.; Ye, V.; Gao, H.; Austin, J.; Li, Z.; and Kanazawa, A. 2024. Shape of motion: 4d reconstruction from a single video. *arXiv*.
- Wang, Z.; Bovik, A. C.; Sheikh, H. R.; and Simoncelli, E. P. 2004. Image quality assessment: from error visibility to structural similarity. *TIP*, 13(4): 600–612.
- Wang, Z.; Cun, X.; Bao, J.; Zhou, W.; Liu, J.; and Li, H. 2022. Uformer: A general u-shaped transformer for image restoration. In *CVPR*, 17683–17693.
- Wu, G.; Yi, T.; Fang, J.; Xie, L.; Zhang, X.; Wei, W.; Liu, W.; Tian, Q.; and Wang, X. 2024. 4d gaussian splatting for real-time dynamic scene rendering. In *CVPR*, 20310–20320.
- Wu, Z.; Yu, C.; Jiang, Y.; Cao, C.; Wang, F.; and Bai, X. 2025. Sc4d: Sparse-controlled video-to-4d generation and motion transfer. In *ECCV*, 361–379. Springer.
- Yan, Z.; Li, C.; and Lee, G. H. 2023. Nerf-ds: Neural radiance fields for dynamic specular objects. In *CVPR*, 8285–8295.
- Yang, X.; Xie, W.; Fu, Y.; Fan, W.; and Dong, X. ??? 4d Gaussian Splatting for High-Fidelity Dynamic Reconstruction of Single-View Scenes. *SSRN*.
- Yang, Z.; Gao, X.; Zhou, W.; Jiao, S.; Zhang, Y.; and Jin, X. 2024. Deformable 3d gaussians for high-fidelity monocular dynamic scene reconstruction. In *CVPR*, 20331–20341.
- Zamir, S. W.; Arora, A.; Khan, S.; Hayat, M.; Khan, F. S.; and Yang, M.-H. 2022. Restormer: Efficient transformer for high-resolution image restoration. In *CVPR*, 5728–5739.
- Zeng, Y.; Jiang, Y.; Zhu, S.; Lu, Y.; Lin, Y.; Zhu, H.; Hu, W.; Cao, X.; and Yao, Y. 2025. Stag4d: Spatial-temporal

anchored generative 4d gaussians. In *ECCV*, 163–179. Springer.

Zhang, G.; Zhu, Y.; Wang, H.; Chen, Y.; Wu, G.; and Wang, L. 2023a. Extracting motion and appearance via inter-frame attention for efficient video frame interpolation. In *CVPR*, 5682–5692.

Zhang, H.; Xie, H.; and Yao, H. 2024. Blur-aware Spatio-temporal Sparse Transformer for Video Deblurring. In *CVPR*, 2673–2681.

Zhang, K.; Luo, W.; Zhong, Y.; Ma, L.; Liu, W.; and Li, H. 2018a. Adversarial spatio-temporal learning for video deblurring. *TIP*, 28(1): 291–301.

Zhang, R.; Isola, P.; Efros, A. A.; Shechtman, E.; and Wang, O. 2018b. The unreasonable effectiveness of deep features as a perceptual metric. In *CVPR*, 586–595.

Zhang, Z.; Liu, Z.; Tan, P.; Zeng, B.; and Liu, S. 2023b. Minimum latency deep online video stabilization. In *ICCV*, 23030–23039.

Zhang, Z.; Xu, R.; Liu, M.; Yan, Z.; and Zuo, W. 2022. Self-supervised image restoration with blurry and noisy pairs. *NeurIPS*, 35: 29179–29191.

Zhang, Z.; Zhang, S.; Wu, R.; Yan, Z.; and Zuo, W. 2024. Bracketing is all you need: Unifying image restoration and enhancement tasks with multi-exposure images. *ICLR*.

Zhao, L.; Wang, P.; and Liu, P. 2024. Bad-gaussians: Bundle adjusted deblur gaussian splatting. *arXiv*.

Zhong, Z.; Cao, M.; Ji, X.; Zheng, Y.; and Sato, I. 2023a. Blur interpolation transformer for real-world motion from blur. In *CVPR*, 5713–5723.

Zhong, Z.; Gao, Y.; Zheng, Y.; and Zheng, B. 2020. Efficient spatio-temporal recurrent neural network for video deblurring. In *ECCV*, 191–207. Springer.

Zhong, Z.; Gao, Y.; Zheng, Y.; Zheng, B.; and Sato, I. 2023b. Real-world video deblurring: A benchmark dataset and an efficient recurrent neural network. *IJCV*, 131(1): 284–301.

Zhou, S.; Zhang, J.; Zuo, W.; Xie, H.; Pan, J.; and Ren, J. S. 2019. Davanet: Stereo deblurring with view aggregation. In *CVPR*, 10996–11005.

Zhu, R.; Liang, Y.; Chang, H.; Deng, J.; Lu, J.; Yang, W.; Zhang, T.; and Zhang, Y. 2024. MotionGS: Exploring Explicit Motion Guidance for Deformable 3D Gaussian Splatting. *arXiv*.

Supplementary Material

The content of the supplementary material involves:

- Structure of camera motion predictor in Sec.A.
- Other regularization terms in Sec.B.
- More comparison results in Sec.C.
- More ablation results in Sec.D.

A Structure of Camera Motion Predictor

The structure of camera motion predictor is provided in fig. 4. It first embeds the camera pose \mathbf{P}_t to a higher dimensional space using high frequency encoder (Mildenhall et al. 2021). Then, three FC blocks are stacked, each consisting of an FC layer followed by a ReLU operation. Finally, we deploy two heads to predict the camera pose at exposure start and end (*i.e.*, $\mathbf{P}_{t,1}$ and $\mathbf{P}_{t,N}$), respectively.

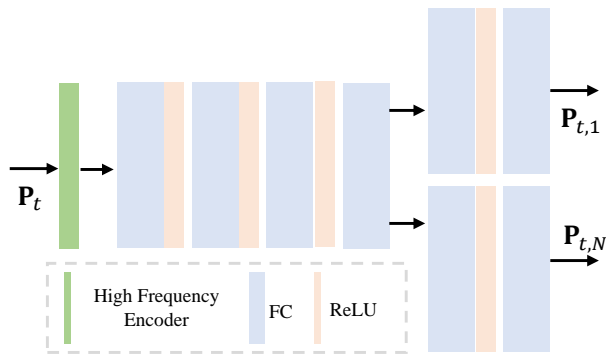


Figure 4: Structure of camera motion predictor.

B Other Regularization Terms

Following Shape-of-Motion (Wang et al. 2024), we use some other regularization terms \mathcal{L}_{oth} to help reconstruct 3D motion better, including mask regularization \mathcal{L}_{mask} , 2D tracks regularization \mathcal{L}_{track} and distance-preserving regularization \mathcal{L}_{rigid} .

Specifically, we render the masks within the exposure time $\{\hat{\mathbf{M}}_{t,i}\}_{i=1}^N$ to indicate dynamic areas. To supervise the training, we synthesize the mask $\hat{\mathbf{M}}_t^B$ for the synthetic blurry image $\hat{\mathbf{B}}_t$ as,

$$\hat{\mathbf{M}}_t^B(u, v) = \max\{\hat{\mathbf{M}}_{t,1}(u, v), \hat{\mathbf{M}}_{t,2}(u, v), \dots, \hat{\mathbf{M}}_{t,N}(u, v)\}. \quad (16)$$

(u, v) is the pixel location. The mask regularization \mathcal{L}_{mask} can be written as,

$$\mathcal{L}_{mask} = \mathcal{L}_1(\hat{\mathbf{M}}_t^B, \mathbf{M}_t), \quad (17)$$

where \mathbf{M}_t is the mask obtained by applying SAM2 (Ravi et al. 2024) to the ground truth blurry frame. Besides, we render the 2D tracks $\hat{\mathbf{U}}_{t \rightarrow t'}$ from a pair of randomly sampled query time t and target time t' . We supervise it by the lifted long-range 2D tracks $\mathbf{U}_{t \rightarrow t'}$ that are extracted from TAPIR (Doersch et al. 2023), *i.e.*,

$$\mathcal{L}_{track} = \mathcal{L}_1(\hat{\mathbf{U}}_{t \rightarrow t'}, \mathbf{U}_{t \rightarrow t'}). \quad (18)$$

Finally, we enforce a distance-preserving loss \mathcal{L}_{rigid} between randomly sampled dynamic Gaussians and their J -nearest neighbors. Let \mathbf{x}_t and $\mathbf{x}_{t'}$ denote the position of a Gaussian at time t and t' , and $\mathcal{C}_J(\mathbf{x}_t)$ denote the set of J -nearest neighbors of \mathbf{x}_t . \mathcal{L}_{rigid} can be written as,

$$\mathcal{L}_{rigid} = \|\text{dist}(\hat{\mathbf{x}}_t, \mathcal{C}_J(\mathbf{x}_t)) - \text{dist}(\hat{\mathbf{x}}_{t'}, \mathcal{C}_J(\mathbf{x}_{t'}))\|_2^2. \quad (19)$$

dist measures the Euclidean distance.

Overall, \mathcal{L}_{oth} can be written as,

$$\mathcal{L}_{oth} = \lambda_{mask}\mathcal{L}_{mask} + \lambda_{track}\mathcal{L}_{track} + \lambda_{rigid}\mathcal{L}_{rigid}. \quad (20)$$

λ_{mask} , λ_{track} and λ_{rigid} are set to 1, 2, and 2, respectively.

C More Comparison Results

fig. 6 shows some examples of real-world videos captured by the Redmi K50 Ultra smartphone. We evaluate methods on four tasks, *i.e.*, novel-view synthesis, deblurring, frame interpolation, and video stabilization. Per-scene results for novel-view synthesis are summarized in table 7, table 8, table 9 and table 10. Rendering speed comparisons are in table 11. More visual comparisons for novel-view synthesis are in fig. 8 and fig. 9. They show that our Deblur4DGS produces more photo-realistic details and fewer visual artifacts. Besides, table 12, table 14 and table 16 summarize the results for deblurring, frame interpolation, and video stabilization on synthetic videos. table 13, table 15, and table 17 summarize those on real-world videos. Deblur4DGS outperforms state-of-the-art 4D reconstruction methods and has competitive capabilities in comparison with task-specific video processing models trained in a supervised manner. Furthermore, visual results for deblurring in fig. 10 show that compared with 4D reconstruction methods, Deblur4DGS produces sharper contents. We provide some videos in the local HTML file.

D More Ablation Results

Visual results in fig. 5 validate the effectiveness of the proposed regularization terms. Without these regularization terms, notable artifacts appear in dynamic areas. By regularizing the object motion within the exposure time distinguished, \mathcal{L}_e improves performance. Besides, \mathcal{L}_{mfc} and \mathcal{L}_{mrc} additionally regularize multi-frame and multi-resolution consistency respectively, helping to alleviate artifacts. In addition, visual results in fig. 7 validate the effectiveness of blur-aware variable (BAV) canonical Gaussians.



(a) Blurry (b) Ours (w/o \mathcal{L}_{reg}) (c) Ours (w/o \mathcal{L}_e) (d) Ours (w/o \mathcal{L}_{mfc}) (e) Ours (w/o \mathcal{L}_{mrc}) (f) Ours (w/ \mathcal{L}_{reg}) (g) Sharp GT

Figure 5: Effect of regularization terms \mathcal{L}_{reg} . \mathcal{L}_{reg} includes exposure regularization \mathcal{L}_e , multi-frame consistency regularization \mathcal{L}_{mfc} , and multi-resolution consistency regularization \mathcal{L}_{mrc} .

Table 7: Per-Scene results for novel view synthesis on 288×512 synthetic data.

Methods	PSNR \uparrow /SSIM \uparrow /LPIPS \downarrow								
	Skating	Seesaw	Street	Basketball	Children	Sailor	Third	Man	Women
DeformableGS	16.74/0.557/0.482	18.27/0.695/0.237	12.13/0.529/0.587	15.34/0.645/0.306	15.04/0.598/0.472	12.89/0.491/0.539	16.91/0.725/0.284	19.48/0.747/0.273	14.66/0.618/0.257
4DGaussians	24.31/0.870/0.130	24.42/0.887/0.104	17.58/0.605/0.326	25.32/0.897/0.117	18.96/0.691/0.344	18.98/0.722/0.323	27.47/0.937/0.089	24.49/0.872/0.136	16.32/0.735/0.209
E-D3DGS	25.59/0.893/0.111	25.16/0.893/0.111	18.37/0.677/0.275	24.71/0.882/0.129	22.34/0.809/0.255	19.91/0.747/0.300	28.56/0.939/0.087	24.52/0.873/0.137	18.67/0.755/0.185
Shape-of-Motion	30.95/0.959/0.088	26.91/0.929/0.086	28.56/0.947/0.073	23.31/0.865/0.180	23.31/0.841/0.306	22.07/0.894/0.190	29.89/0.960/0.074	25.82/0.947/0.147	23.72/0.851/0.151
SplineGS	28.55/0.948/0.095	28.48/0.953/0.075	24.55/0.924/0.082	26.02/0.915/0.129	22.21/0.777/0.438	25.31/0.876/0.232	29.65/0.960/0.076	25.89/0.908/0.149	23.83/0.848/0.129
DyBluRF	29.54/0.935/0.076	26.46/0.936/0.080	26.40/0.938/0.085	26.24/0.907/0.059	25.32/0.903/0.111	25.27/0.905/0.123	28.57/0.937/0.070	24.40/0.926/0.103	22.23/0.860/0.105
BARD-GS	29.78/0.940/0.060	27.12/0.944/0.057	28.25/0.939/0.067	26.25/0.923/0.083	25.67/0.910/0.109	25.21/0.901/0.111	29.56/0.961/0.051	26.87/0.934/0.067	23.56/0.858/0.086
Deblur4DGS (Ours)	30.84/0.965/0.047	28.45/0.954/0.049	29.01/0.953/0.048	27.00/0.932/0.065	26.05/0.916/0.087	25.72/0.910/0.097	29.82/0.964/0.047	28.53/0.957/0.032	23.55/0.865/0.066

Table 8: Per-Scene results for novel view synthesis on 720×1280 synthetic data.

Methods	PSNR \uparrow /SSIM \uparrow /LPIPS \downarrow								
	Skating	Seesaw	Street	Basketball	Children	Sailor	Third	Man	Women
DeformableGS	16.58/0.708/0.482	17.36/0.739/0.332	11.53/0.605/0.673	15.34/0.730/0.324	16.15/0.744/0.587	12.36/0.612/0.588	17.46/0.786/0.345	19.50/0.782/0.323	14.22/0.646/0.369
4DGaussians	23.75/0.880/0.203	23.84/0.886/0.190	17.99/0.740/0.344	20.66/0.827/0.193	22.32/0.830/0.398	18.89/0.784/0.382	26.99/0.930/0.168	23.62/0.852/0.210	17.16/0.752/0.286
E-D3DGS	25.09/0.897/0.186	24.32/0.891/0.183	18.04/0.764/0.353	23.87/0.873/0.172	22.27/0.833/0.394	19.05/0.791/0.376	27.37/0.927/0.181	23.71/0.853/0.208	18.43/0.771/0.276
Shape-of-Motion	30.11/0.946/0.169	25.57/0.913/0.200	27.87/0.939/0.139	23.21/0.876/0.224	24.12/0.860/0.488	23.76/0.864/0.355	28.92/0.948/0.156	24.84/0.879/0.238	23.88/0.853/0.248
SplineGS	28.30/0.938/0.176	27.27/0.936/0.174	24.07/0.919/0.146	24.79/0.895/0.199	22.24/0.790/0.440	20.93/0.816/0.472	28.79/0.948/0.155	24.76/0.875/0.240	23.06/0.833/0.268
DyBluRF	29.14/0.915/0.134	26.56/0.930/0.128	26.01/0.928/0.135	25.84/0.902/0.147	25.12/0.893/0.245	24.97/0.903/0.220	27.17/0.928/0.124	24.30/0.919/0.151	22.23/0.851/0.153
BARD-GS	29.30/0.930/0.122	25.89/0.935/0.125	27.98/0.942/0.122	25.96/0.912/0.116	24.29/0.831/0.250	24.70/0.880/0.193	28.90/0.948/0.112	25.84/0.920/0.101	24.20/0.890/0.113
Deblur4DGS (Ours)	30.77/0.956/0.093	27.52/0.942/0.107	28.22/0.944/0.093	26.93/0.931/0.109	25.68/0.905/0.235	24.91/0.897/0.185	28.96/0.955/0.104	28.05/0.948/0.064	23.50/0.865/0.114

Table 9: Per-Scene results for novel view synthesis on real-world videos captured by Redmi K50 Ultra.

Methods	CLIPQA \uparrow /MUSIQ \uparrow					
	Girl	Running	Boy	Walking	Airport	Bookshop
DeformableGS	0.204/26.941	0.190/22.321	0.266/25.099	0.246/30.193	0.301/23.545	0.219/27.321
4DGaussians	0.220/31.099	0.201/26.140	0.270/21.963	0.237/27.717	0.267/22.642	0.224/29.499
E-D3DGS	0.232/30.962	0.219/25.331	0.287/23.929	0.257/30.423	0.282/23.707	0.267/33.447
Shape-of-Motion	0.267/31.979	0.234/22.515	0.322/20.214	0.241/27.609	0.344/18.093	0.252/26.827
SplineGS	0.228/ 48.300	0.207/ 34.833	0.308/29.323	0.248/26.299	0.299/25.081	0.222/28.295
DyBluRF	0.169/21.756	0.160/29.160	0.303/31.051	0.321/25.824	0.218/ 38.048	0.257/ 42.090
BARD-GS	0.245/46.379	0.226/30.318	0.349/35.593	0.270/ 33.241	0.287/30.259	0.351/37.244
Deblur4DGS (Ours)	0.315/43.292	0.250/31.654	0.467/38.602	0.342/37.978	0.433/30.573	0.327/38.435

Table 10: Per-Scene results for **novel view synthesis** on real-world videos from BARD-GS (Lu et al. 2025).

Methods	PSNR↑/SSIM↑/LPIPS↓ card	PSNR↑/SSIM↑/LPIPS↓ cube-desk	PSNR↑/SSIM↑/LPIPS↓ kitchen	PSNR↑/SSIM↑/LPIPS↓ micro-lab	PSNR↑/SSIM↑/LPIPS↓ pen-spinning	PSNR↑/SSIM↑/LPIPS↓ poster
DeformableGS	13.85/0.762/0.394	13.95/0.749/0.394	16.04/0.812/0.357	17.21/0.769/0.322	15.33/0.677/0.369	21.74/0.865/0.317
4DGaussians	<u>22.39/0.899/0.156</u>	24.69/0.896/0.207	21.05/0.876/0.280	21.34/0.852/0.249	18.98/0.766/0.380	30.34/0.945/0.163
E-D3DGS	21.65/0.882/0.155	24.83/0.899/0.215	21.52/0.888/0.285	22.95/0.886/0.228	18.91/0.769/0.391	<u>30.55/0.946/0.168</u>
Shape-of-Motion	18.98/0.863/0.340	21.26/0.884/0.308	21.26/0.885/0.308	24.80/0.882/0.234	15.06/0.721/0.567	30.50/0.950/0.154
SplineGS	22.64/0.902/0.128	24.67/0.893/0.262	24.54/0.913/0.256	<u>25.86/0.897/0.227</u>	21.19/0.826/0.253	30.57/0.951/0.159
DyBluRF	20.73/0.841/0.169	21.41/0.825/0.179	21.78/0.849/0.191	27.04/0.863/0.116	21.60/0.652/0.345	30.15/0.925/0.088
BARD-GS	20.54/0.851/0.211	22.39/0.863/0.203	21.49/0.883/0.190	24.41/0.881/0.150	<u>21.45/0.812/0.216</u>	29.54/0.954/0.090
Deblur4DGS (Ours)	21.56/0.882/0.189	<u>24.70/0.897/0.155</u>	<u>24.31/0.916/0.144</u>	<u>23.27/0.863/0.145</u>	19.89/0.737/0.243	<u>29.38/0.945/0.089</u>
Methods	PSNR↑/SSIM↑/LPIPS↓ rubik-cube	PSNR↑/SSIM↑/LPIPS↓ shark-spin	PSNR↑/SSIM↑/LPIPS↓ tennis-ball	PSNR↑/SSIM↑/LPIPS↓ toycar	PSNR↑/SSIM↑/LPIPS↓ walk	PSNR↑/SSIM↑/LPIPS↓ windmill
DeformableGS	14.38/0.827/0.335	18.09/0.837/0.299	15.19/0.708/0.362	13.08/0.768/0.347	16.21/0.787/0.342	15.57/0.800/0.359
4DGaussians	20.23/0.905/0.188	23.11/0.896/0.221	<u>21.35/0.838/0.189</u>	19.10/0.887/0.155	25.01/0.905/0.163	20.62/0.792/0.257
E-D3DGS	20.10/0.908/0.200	23.07/0.897/0.235	22.52/0.852/0.185	<u>20.15/0.890/0.145</u>	24.06/0.899/0.204	21.50/0.894/0.204
Shape-of-Motion	15.10/0.847/0.354	11.37/0.724/0.468	20.63/0.830/0.182	18.32/0.878/0.168	23.91/0.893/0.222	21.70/0.890/0.231
SplineGS	20.78/0.907/0.196	<u>25.08/0.910/0.251</u>	20.47/0.831/0.173	22.35/0.928/0.095	<u>25.25/0.909/0.178</u>	<u>23.67/0.915/0.185</u>
DyBluRF	19.65/0.829/0.214	23.87/0.889/0.194	20.99/0.731/0.224	19.83/0.845/0.162	24.46/0.821/0.180	20.89/0.784/0.249
BARD-GS	21.09/0.900/0.169	23.90/0.901/0.252	19.16/0.745/0.196	19.31/0.878/0.191	24.51/0.895/0.138	24.48/0.927/0.123
Deblur4DGS (Ours)	<u>21.05/0.917/0.156</u>	25.09/0.915/0.162	19.96/0.777/0.179	18.80/0.864/0.212	25.60/0.916/0.112	<u>23.55/0.916/0.141</u>

Table 11: Rendering speed comparisons on 720×1080 images.

Methods	DeformableGS	4DGaussians	E-D3DGS	Shape-of-Motion	SplineGS	DyBluRF	BARD-GS	Deblur4DGS
FPS	<u>98.03</u>	56.82	81.31	96.22	130.12	0.04	80.43	96.22

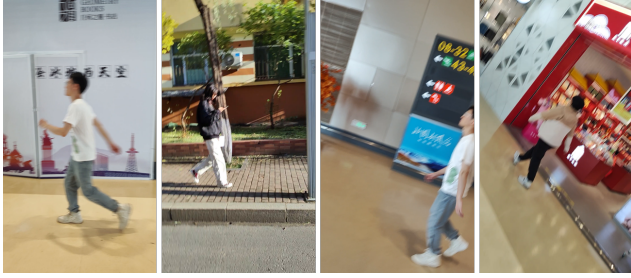


Figure 6: Some examples of our captured real-world blurry videos by the Redmi K50 Ultra smartphone.

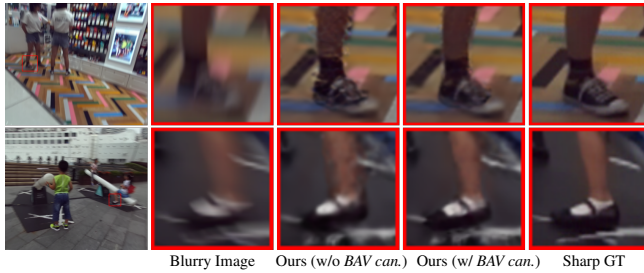


Figure 7: Effect of BAV canonical Gaussians.

Table 12: **deblurring** results on synthetic datasets.

Methods	PSNR \uparrow /SSIM \uparrow /LPIPS \downarrow 288 \times 512	PSNR \uparrow /SSIM \uparrow /LPIPS \downarrow 720 \times 1080
Restormer	35.45 / 0.984 / 0.023	34.66 / 0.976 / 0.037
DSTNet	34.79 / 0.981 / 0.020	33.90 / 0.973 / 0.034
BSSTNet	35.51 / 0.985 / 0.016	34.89 / 0.980 / 0.025
DeformableGS	26.88 / 0.866 / 0.177	25.53 / 0.849 / 0.239
4DGaussians	29.21 / 0.916 / 0.132	28.41 / 0.914 / 0.201
E-D3DGS	29.79 / 0.932 / 0.122	28.35 / 0.914 / 0.206
Shape-of-Motion	28.11 / 0.935 / 0.150	27.27 / 0.912 / 0.240
SplineGS	27.09 / 0.916 / 0.153	26.26 / 0.908 / 0.222
DyBluRF	29.44 / 0.947 / 0.081	28.31 / 0.916 / 0.127
BARD-GS	29.98 / 0.949 / 0.080	28.28 / 0.919 / 0.129
Deblur4DGS (Ours)	30.36 / 0.955 / 0.078	29.53 / 0.929 / 0.109

Table 13: **deblurring** results on real-world datasets.

Methods	CLIPQA \uparrow /MUSIQ \uparrow Redmi	CLIPQA \uparrow /MUSIQ \uparrow BARD-GS
Restormer	0.254 / 37.299	0.278 / 40.378
DSTNet	0.260 / 40.213	0.217 / 27.741
BSSTNet	0.266 / 47.639	0.280 / 45.798
DeformableGS	0.249 / 26.894	0.325 / 31.186
4DGaussians	0.241 / 27.302	0.337 / 31.409
E-D3DGS	0.260 / 28.198	0.317 / 26.567
Shape-of-Motion	0.277 / 24.846	0.311 / 27.872
SplineGS	0.263 / 32.044	0.329 / 36.453
DyBluRF	0.236 / 35.240	0.295 / 34.792
BARD-GS	0.290 / 35.704	0.392 / 39.983
Deblur4DGS (Ours)	0.358 / 37.051	0.409 / 41.318

Table 14: **frame interpolation** results on synthetic datasets.

Methods	CLIPQA \uparrow / MUSIQ \uparrow 288 \times 512	CLIPQA \uparrow / MUSIQ \uparrow 720 \times 1080
RIFE	0.178 / 41.189	0.156 / 31.274
EMAVFI	0.179 / 39.784	0.174 / 31.031
VIDUE	0.263 / 61.333	0.186 / 49.195
DeformableGS	0.169 / 38.312	0.172 / 29.264
4DGaussians	0.171 / 41.018	0.180 / 32.032
E-D3DGS	0.173 / 39.809	0.184 / 31.145
Shape-of-Motion	0.176 / 38.871	0.202 / 31.255
SplineGS	0.184 / 44.963	0.194 / 37.788
DyBluRF	0.149 / 50.689	0.125 / 35.456
BARD-GS	0.198 / 51.123	0.196 / 38.256
Deblur4DGS (Ours)	0.201 / 52.852	0.207 / 39.721

Table 15: **frame interpolation** results on real-world datasets.

Methods	CLIPQA \uparrow / MUSIQ \uparrow Redmi	CLIPQA \uparrow / MUSIQ \uparrow BARD-GS
RIFE	0.257 / 30.053	0.300 / 30.781
EMAVFI	0.258 / 27.025	0.318 / 30.082
VIDUE	0.273 / 40.332	0.346 / 45.782
DeformableGS	0.242 / 25.972	0.320 / 30.504
4DGaussians	0.234 / 26.923	0.333 / 31.010
E-D3DGS	0.249 / 26.425	0.314 / 25.974
Shape-of-Motion	0.286 / 28.078	0.313 / 27.809
SplineGS	0.272 / 33.553	0.330 / 37.887
DyBluRF	0.230 / 35.523	0.291 / 34.217
BARD-GS	0.301 / 36.003	0.390 / 40.002
Deblur4DGS (Ours)	0.360 / 37.224	0.416 / 41.933

Table 16: **video stabilization** results on synthetic datasets.

Methods	CLIPQA \uparrow /MUSIQ \uparrow 288 \times 512	CLIPQA \uparrow /MUSIQ \uparrow 720 \times 1080
MeshFlow	0.154 / 34.416	0.136 / 31.105
NNDVS	0.180 / 43.003	0.128 / 32.262
DeformableGS	0.169 / 37.978	0.173 / 28.811
4DGaussians	0.151 / 41.662	0.177 / 32.623
E-D3DGS	0.178 / 40.773	0.185 / 32.362
Shape-of-Motion	0.175 / 38.971	0.202 / 31.183
SplineGS	0.184 / 43.834	0.185 / 36.993
DyBluRF	0.148 / 32.091	0.126 / 36.115
BARD-GS	0.196 / 51.479	0.193 / 38.472
Deblur4DGS (Ours)	0.201 / 53.060	0.206 / 39.786

Table 17: **video stabilization** results on real-world datasets.

Methods	CLIPQA \uparrow /MUSIQ \uparrow Redmi	CLIPQA \uparrow /MUSIQ \uparrow BARD-GS
MeshFlow	0.331 / 28.650	0.347 / 33.324
NNDVS	0.254 / 28.844	0.317 / 33.674
DeformableGS	0.235 / 25.309	0.318 / 30.144
4DGaussians	0.231 / 26.472	0.328 / 31.487
E-D3DGS	0.253 / 27.454	0.317 / 26.863
Shape-of-Motion	0.269 / 24.142	0.311 / 27.875
SplineGS	0.259 / 31.766	0.328 / 36.634
DyBluRF	0.260 / 34.117	0.292 / 34.319
BARD-GS	0.295 / 35.892	0.387 / 39.275
Deblur4DGS (Ours)	0.352 / 36.351	0.408 / 41.317

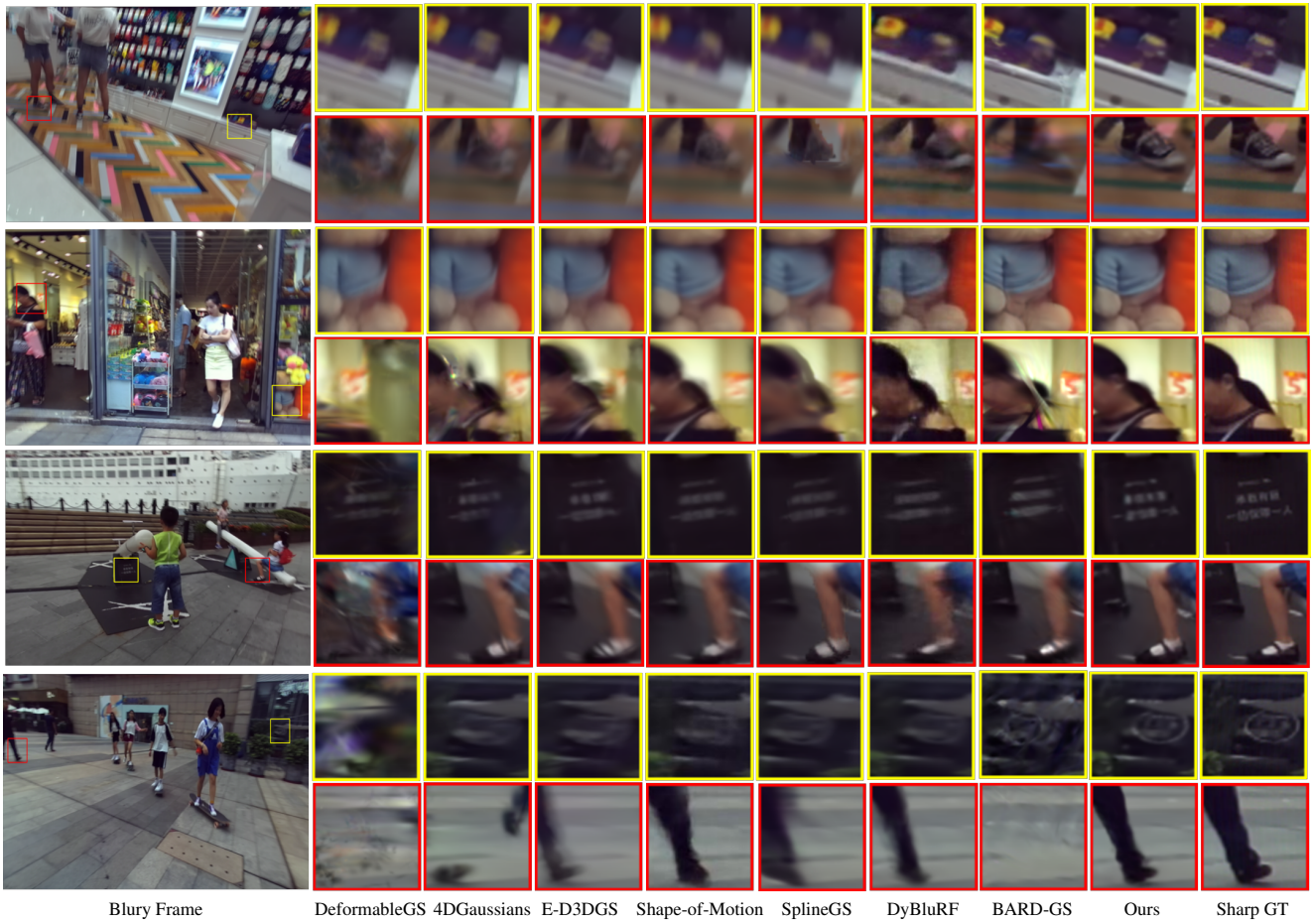


Figure 8: Visual comparisons of novel-view synthesis on the 720×1080 images. Our method produces more photo-realistic details in both static and dynamic areas, as marked with yellow and red boxes respectively.

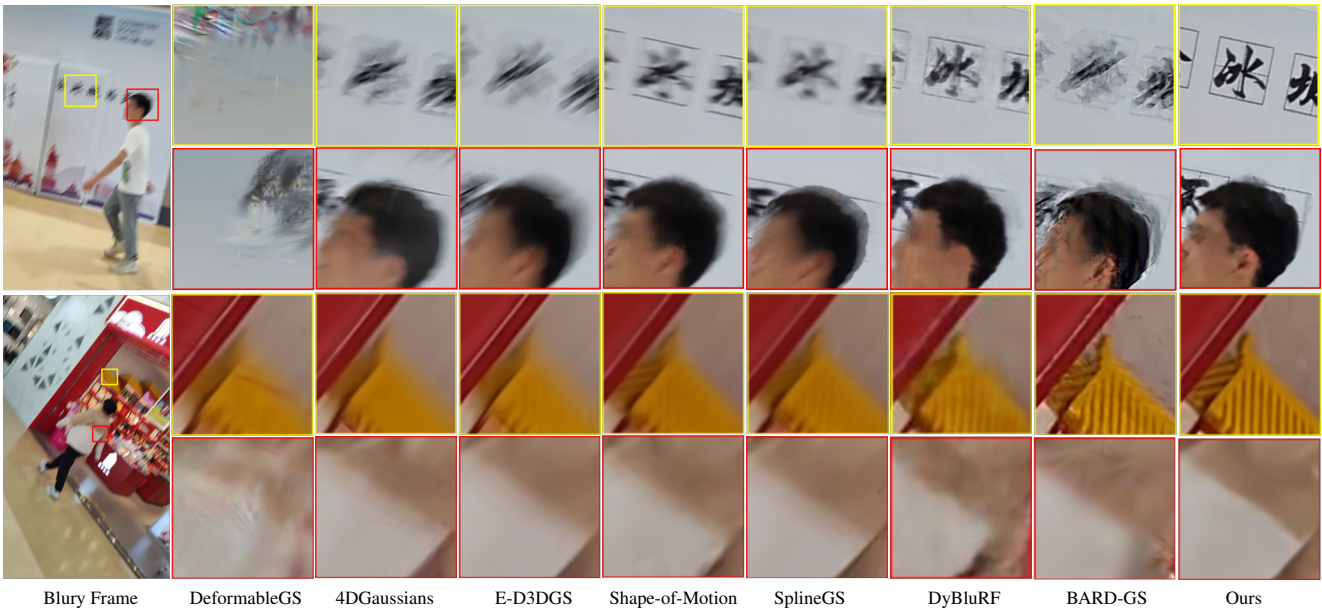


Figure 9: Visual comparisons of novel-view synthesis on real-world videos. Our method produces more photo-realistic details in both static and dynamic areas, as marked with yellow and red boxes respectively.

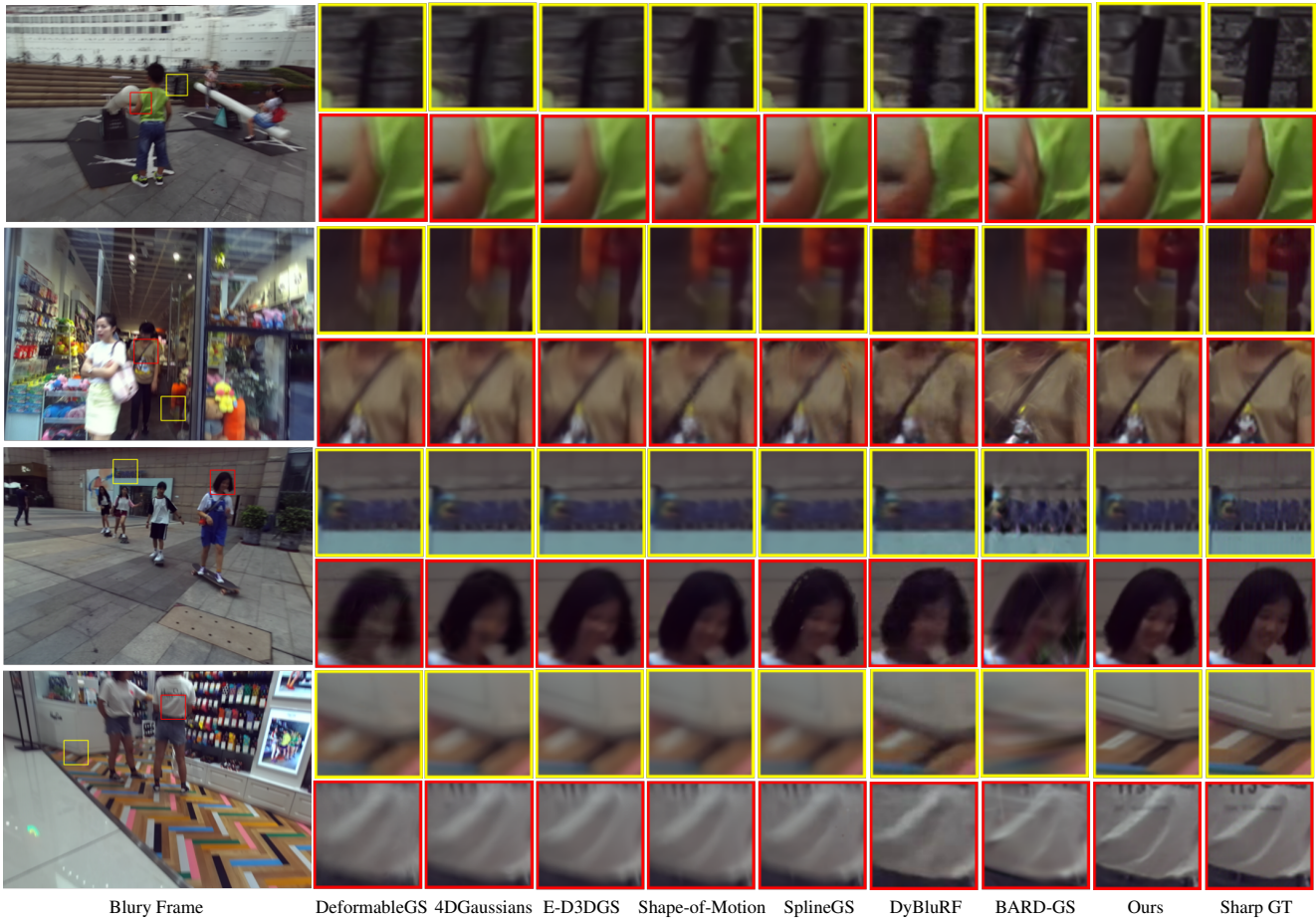


Figure 10: Visual comparisons of deblurring on the 720×1080 images. Compared with 4D reconstruction-based methods, Deblur4DGS produces sharper contents and fewer artifacts in both static and dynamic areas, as marked with yellow and red boxes respectively.